Melt generation, crystallization, and extraction beneath segmented oceanic transform faults

P. M. Gregg,[1,2] M. D. Behn,[3] J. Lin,[3] and T. L. Grove[4]

[1]   We examine mantle melting, fractional crystallization, and melt extraction beneath fast slipping, segmented oceanic transform fault systems. Three-dimensional mantle flow and thermal structures are calculated using a temperature-dependent rheology that incorporates a viscoplastic approximation for brittle deformation in the lithosphere. Thermal solutions are combined with the near-fractional, polybaric melting model of Kinzler and Grove (1992a, 1992b, 1993) to determine extents of melting, the shape of the melting regime, and major element melt composition. We investigate the mantle source region of intratransform spreading centers (ITSCs) using the melt migration approach of Sparks and Parmentier (1991) for two end-member pooling models: (1) a wide pooling region that incorporates all of the melt focused to the ITSC and (2) a narrow pooling region that assumes melt will not migrate across a transform fault or fracture zone. Assuming wide melt pooling, our model predictions can explain both the systematic crustal thickness excesses observed at intermediate and fast slipping transform faults as well as the deeper and lower extents of melting observed in the vicinity of several transform systems. Applying these techniques to the Siqueiros transform on the East Pacific Rise we find that both the viscoplastic rheology and wide melt pooling are required to explain the observed variations in gravity inferred crustal thickness. Finally, we show that mantle potential temperature $T_p = 1350°C$ and fractional crystallization at depths of $9-15.5$ km fit the majority of the major element geochemical data from the Siqueiros transform fault system.

Citation: Gregg, P. M., M. D. Behn, J. Lin, and T. L. Grove (2009), Melt generation, crystallization, and extraction beneath segmented oceanic transform faults, *J. Geophys. Res.*, *114*, B11102, doi:10.1029/2008JB006100.

1.   Introduction

[2]   Transform faults are a first-order feature of the global mid-ocean ridge system. Transform fault offsets range from 50 km to >350 km in length and greatly influence thermal structure, mantle flow, melting, and crystallization at mid-ocean ridges [*Fox and Gallo*, 1984; *Parmentier and Forsyth*, 1985; *Phipps Morgan and Forsyth*, 1988]. Investigations of transform faults suggest that the cold, thick lithosphere at fault offsets effectively divides mid-ocean ridges into unique segments, focusing melt toward segment centers and prohibiting shallow across-transform mantle flow. Gravity and seismic studies at slow spreading ridges indicate along-segment variations in crustal thickness with enhanced magma accretion at ridge segment centers and crustal thinning toward transform and nontransform offsets

[*Kuo and Forsyth*, 1988; *Lin et al.*, 1990; *Lin and Phipps Morgan*, 1992; *Tolstoy et al.*, 1993; *Detrick et al.*, 1995; *Escartin and Lin*, 1995; *Canales et al.*, 2000; *Hooft et al.*, 2000]. Juxtaposing the cold, thick lithosphere of a transform fault next to a warm steady state ridge segment also influences the compositions of the erupted lavas. A geochemical signal in the lavas erupted adjacent to transform faults has been noted by several investigators [*Bender et al.*, 1978, 1984; *Langmuir and Bender*, 1984; *Langmuir et al.*, 1986; *Reynolds et al.*, 1992; *Reynolds and Langmuir*, 1997]. This effect has been attributed to the influence of the cooler mantle surrounding the transform fault system, promoting lower extents of melting near the segment ends.

[3]   Oceanic transform faults along fast spreading ridges are often characterized by segmentation by intratransform spreading centers (ITSCs) [*Menard*, 1967; *Menard and Atwater*, 1969; *Searle*, 1983; *Fox and Gallo*, 1984]. In the case of several transform fault systems along the fast spreading East Pacific Rise (EPR) (e.g., Siqueiros, Quebrada, Discovery, Gofar, and Garrett transform systems, Figure 1a), fresh basalts sampled on ITSCs and detailed magnetic data suggest active accretion [*Fornari et al.*, 1989; *Carbotte and Macdonald*, 1992; *Hekinian et al.*, 1992, 1995; *Perfit et al.*, 1996; *Nagle et al.*, 2007]. Segmentation of oceanic transform faults is generally thought to be the result of transtensional forces imposed on the transform fault zone by plate

[1]MIT/WHOI Joint Program, Woods Hole Oceanographic Institution, Woods Hole, Massachusetts, USA.

[2]Now at Department of Geosciences, Oregon State University, Corvallis, Oregon, USA.

[3]Department of Geology and Geophysics, Woods Hole Oceanographic Institution, Woods Hole, Massachusetts, USA.

[4]Department of Earth, Atmospheric, and Planetary Sciences, Massachusetts Institute of Technology, Cambridge, Massachusetts, USA.
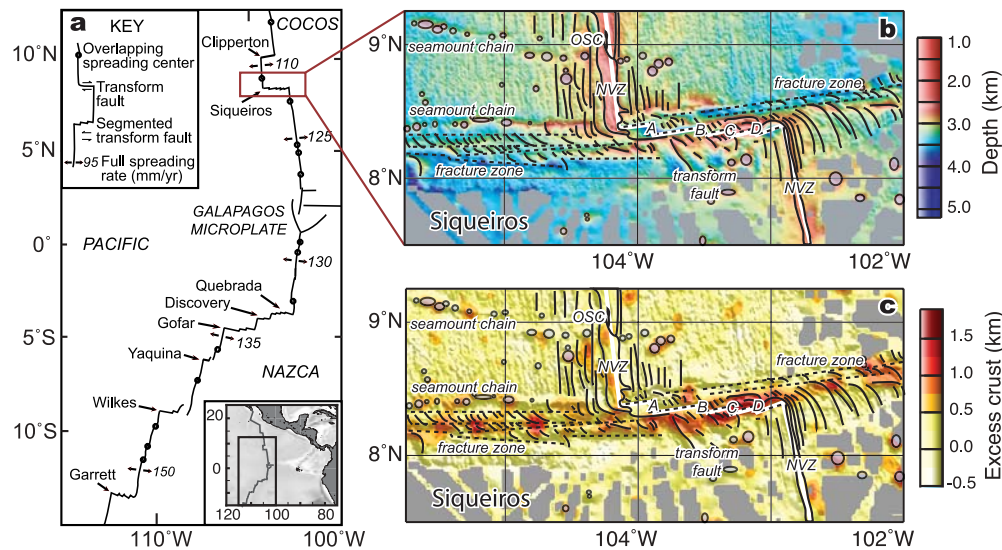
Figure 1. Comparison of bathymetry and crustal thickness predictions for Siqueiros transform fault along the EPR. (a) EPR segmentation and location of transform faults. Note that all of the transform faults, except for Clipperton, are segmented by at least one ITSC. (b) Siqueiros transform fault bathymetry with structural interpretation [*Fornari et al.*, 1989]. Solid black lines indicate the seafloor fabric, circles show locations of seamounts, and dashed black lines show the locations of the fracture zones and transform fault. (c) Lateral variations in crustal thickness derived from residual mantle Bouguer gravity calculations [*Gregg et al.*, 2007]. Excess crust is defined as the deviation for the reference crustal thickness of 6 km, assuming seawater, crust, and mantle densities of 1030, 2730, and 3300 kg m^{-3}, respectively.

motion reorganization [*Menard and Fisher*, 1958; *Menard and Atwater*, 1969]. Specifically, the change in spreading direction enables mantle upwelling beneath the transform fault domain and the formation of small ITSCs [*Searle*, 1983; *Fornari et al.*, 1989; *Pockalny*, 1997; *Pockalny et al.*, 1997].

[4] Recent analyses of residual mantle Bouguer gravity anomalies along several intermediate and fast slipping transform fault systems indicate that for spreading rates >~50 mm/yr full-rate, the observed residual mantle Bouguer gravity anomalies within the transform fault domain are more negative than their adjacent ridge segments [*Gregg et al.*, 2007], indicating a mass deficit within these settings. If the mass deficit is due to crustal thickness variations, these findings contradict the classic model for transform faults as regions of thin crust relative to adjacent ridge segments. One possible explanation for these observations is that long-lived ITSCs may focus upwelling mantle and melt beneath the transform domain, warm the fault system, and result in excess crustal accretion. As we show below, the apparent contradiction posed by observations of both thicker crust and lower extents of melting within fast slipping transform faults is likely a consequence of the shape of the melt region that feeds the ITSCs.

[5] In this study, we develop 3-D models of a ridge-transform-ridge system to explore the effect of transform fault segmentation on mantle flow, melt generation, and melt extraction. Recent modeling investigations of ridge-transform-ridge systems illustrate the importance of incorporating brittle weakening of the lithosphere into thermal models of these settings [*Behn et al.*, 2007]. We compare the results of models with both a constant viscosity rheol-

ogy and a temperature-dependent viscoplastic rheology that approximates brittle deformation [*Chen and Morgan*, 1990; *Behn et al.*, 2007]. Calculated thermal structures are used in conjunction with the fractional melting model of *Kinzler and Grove* [1992a, 1992b, 1993] and fractional crystallization model of *Yang et al.* [1996] to calculate crustal thickness and predict major element lava compositions. First, we investigate a suite of generic 3-D transform fault models segmented by a single ITSC. We find that crustal production is enhanced at ITSCs relative to the adjacent ridge segments because melts are pooled at the transform from a large region of the mantle. Second, we consider a case appropriate for the Siqueiros transform fault system on the EPR (Figures 1b and 1c) and compare our model-predicted crustal thicknesses and lava compositions to geophysical and geochemical observations in this region.

2. Model Setup

[6] The 3-D mantle flow field and temperature are calculated using the finite element modeling software COMSOL 3.3 Multiphysics, which as been benchmarked for temperature-dependent flow in geologic systems [*van Keken et al.*, 2008]. Mantle flow is driven by the divergence of two surface plates moving apart at a half-spreading rate, U_0 (Figure 2). A stress free boundary is assumed at the base of the model (100 km depth), allowing for convective flux from the mantle below. The sides of the models are also stress free. The temperature at the surface of the model is set to $T_0 = 0°C$ and a mantle potential temperature, T_p, is defined at the surface and then extrapolated along an adiabat to the base of the model. The model geometry is varied to
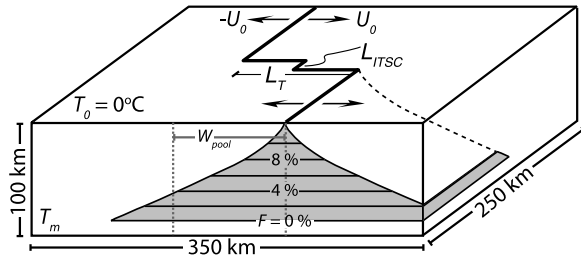
Figure 2. Three-dimensional setup for modeling mantle temperature structure beneath a segmented transform fault. Spreading velocities are imposed at the surface. Other model parameters include spreading rate, U_0; temperatures at the surface, T_0, and at the base of the model box, T_m; the length of transform, L_T; and the length of intratransform spreading center, L_{ITSC}. An example melt region is illustrated with melt fractions, F. The melt pooling width, W_{pool}, is shown between the gray dotted lines.

explore the effect of fault segmentation by imposing a single ITSC of length, L_{ITSC}, which bisects a transform fault of length L_T (Figure 2). Model parameters are given in Table 1, and a list of variables is given in Table 2.

2.1. Numerical Approach

[7] Conservation of mass, momentum, and energy are given by:

$$\nabla \cdot \mathbf{u} = 0, \tag{1}$$

$$\rho \left(\frac{\partial u}{\partial t} + \mathbf{u} \cdot \nabla \mathbf{u} \right) = -\nabla p + \eta_{eff} \nabla^2 \mathbf{u}, \tag{2}$$

$$\rho C_p \mathbf{u} \bullet \nabla T + k \nabla^2 T = 0, \tag{3}$$

respectively, where ρ is the density of the mantle, p is pressure, $\mathbf{u}$ is the velocity field, η_{eff} is the effective mantle viscosity, C_p is the heat capacity, T is temperature, and k is the thermal conductivity.

[8] Mantle flow and temperature are both largely dependent on the assumed mantle viscosity. To explore the importance of incorporating a temperature-dependent viscoplastic rheology, we compare isoviscous solutions to those calculated using a temperature-dependent viscosity that incorporates a viscoplastic approximation for brittle failure [Chen and Morgan, 1990; Behn et al., 2007]. The effective mantle viscosity is defined by:

$$\eta_{eff} = \left(\frac{1}{\eta_{td}} + \frac{1}{\eta_{byr}} + \frac{1}{\eta_{max}} \right)^{-1} \tag{4}$$

where η_{td} is the temperature-dependent viscosity, η_{byr} is a brittle strength approximation using Byerlee's law, and η_{max} is the maximum viscosity (10^{23} Pa · s). The temperature dependence of viscosity is calculated by:

$$\eta_{td} = \eta_0 \exp \left(\frac{Q}{R} \left(\frac{1}{T} - \frac{1}{T_p} \right) \right), \tag{5}$$

where η_0 is the reference viscosity (10^{19} Pa · s), Q is the activation energy, and R is the universal gas constant. The viscosity associated with brittle failure is approximated by [Chen and Morgan, 1990]:

$$\eta_{byr} = \frac{S}{\sqrt{2} \dot{\varepsilon}_{II}}, \tag{6}$$

where $\dot{\varepsilon}_{II}$ is the second invariant of the strain rate tensor, and the maximum shear stress, S, is defined by:

$$S = \frac{2}{5} (p_r - p_w), \tag{7}$$

Table 1. Model Parameters

Parameter	Description	Value
A	Smoothing coefficient for hydrothermal cooling equation	0.75
C_p	Specific heat capacity, J kg^{-1} °K^{-1}	1.25×10^3
η_{max}	Maximum viscosity, Pa s	10^{23}
η_0	Reference viscosity, Pa s	10^{19}
k_0	Reference thermal conductivity, W m^{-1} °K^{-1}	3
L	Latent heat of melting, J kg^{-1}	400×10^3
L_T	Transform fault length, km	100
L_{ITSC}	Intratransform spreading center length, km	5–25
Nu	Nusselt number	1–8
Q	Activation energy, J mol^{-1}	250×10^3
ρ	Reference mantle density, kg m^{-3}	3300
R	Universal gas constant, J mol^{-1} °K^{-1}	8.3114
T_0	Temperature at the surface of the thermal model, °C	0
T_{max}	Maximum temperature of hydrothermal fluid circulation, °C	600
T_p	Mantle potential temperature used in melt models, °C	1300–1400
U_0	Imposed spreading half-rate, mm yr^{-1}	50
W_{pool}	Horizontal length scale for melt migration, km	75–200
z_{max}	Maximum depth of hydrothermal fluid circulation, km	6

Table 2. Variables

| Variable	Description
C_0	Initial oxide concentration
$C_{i,m}$	Concentration of oxide, i, in the melt
$D_{i,s}$	Bulk partition coefficient of oxide, i, in the initial solid
Δt_c	Change in crustal thickness, km
$\dot{\varepsilon}_{II}$	Second invariant of the strain rate tensor, s^{-1}
F	Melt fraction, %
F_c	Melt fraction, cation fraction units
F_{max}	Maximum melt fraction, %
η_{byr}	Brittle strength viscosity, Pa s
η_{td}	Temperature-dependent viscosity, Pa s
η_{eff}	Effective viscosity, Pa s
k	Effective thermal conductivity, W m^{-1} °K^{-1}
p	Pressure of melting, kbar
p_r	Lithostatic pressure, Pa
p_w	Hydrostatic pressure, Pa
$P_{i,m}$	Bulk partition coefficient of oxide, i, in the melt
S	Maximum shear stress, Pa
T	Temperature, °C
T_m	Mantle temperature extrapolated from T_p, °C
T_s	Solidus temperature, °C
$\mathbf{u}$	Velocity field, mm yr^{-1}
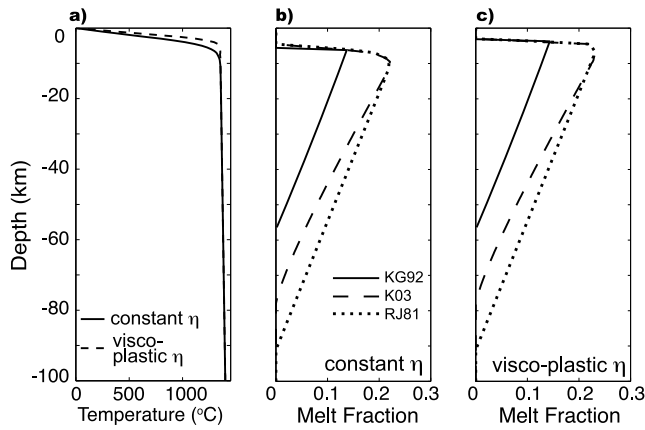
Figure 3. Comparison of melting models for two mantle rheologies. (a) Comparison of mantle temperature sampled beneath the oceanic spreading center for an isoviscous and temperature-dependent viscoplastic rheology. Calculated melt fraction for (b) constant viscosity rheology and (c) viscoplastic model. The effect of latent heat of melting has been incorporated into all melting models. KG92, *Kinzler and Grove* [1992a, 1992b, 1993], the solid line; RJ81, *Reid and Jackson* [1981], the dotted line; and K03, *Katz et al.* [2003], the dashed line. $U_0 = 50$ mm/yr, $T_p = 1350°C$, Nu = 4, and latent heat of melting L = 400 J/kg.

where p_r is the lithostatic pressure and p_w is the hydrostatic pressure.

[9] The incorporation of the viscoplastic rheology promotes focused mantle upwelling and warmer temperatures in areas with high strain rates [*Behn et al.*, 2007]. This effect is most pronounced beneath the ridge axis and transform fault where the imposed surface boundary conditions generate high strain rates. Therefore, models using the viscoplastic rheology result in a warmer thermal structure beneath the ridge axis and transform fault domain than those calculated with a constant viscosity rheology (Figure 3a).

[10] Hydrothermal circulation will promote more efficient heat loss in the crust and upper mantle [*Phipps Morgan et al.*, 1987; *Phipps Morgan and Chen*, 1993; *Baker et al.*, 1996; *Maclennan et al.*, 2005]. This effect is likely to be particularly important at oceanic transform faults where extensive brittle deformation increases permeability and produces pathways for fluids to reach greater depths. We assume that hydrothermal circulation is present at temperatures <600°C and depths <6 km [*Phipps Morgan et al.*, 1987; *Phipps Morgan and Chen*, 1993]. Where hydrothermal circulation is assumed to occur we increase the thermal conductivity by an enhancement factor or Nusselt number, Nu [*Phipps Morgan et al.*, 1987]. Because permeability most likely decreases with depth due to increased confining pressure and temperature, the enhancement in conductivity is assumed to decay exponentially as the depth and temperature approach the cutoff values for fluid circulation:

$$k = k_0 + k_0^**(Nu - 1)* \exp$$
$$\cdot \left(A*\left(1 - \frac{T}{T_{max}}\right)\right)* \exp\left(A*\left(1 - \frac{z}{z_{max}}\right)\right), \quad (8)$$

where k is the effective thermal conductivity, k_0 is the reference thermal conductivity, A is a smoothing factor, T_{max} is the cutoff maximum temperature (600°C), z is depth, and z_{max} is the cutoff maximum depth (6 km).

2.2. Melt Generation and Extraction

[11] Melting within the mantle at mid-ocean ridges is dependent on pressure and temperature as well as the chemical composition of the mantle [*Grove et al.*, 1992; *Langmuir et al.*, 1992; *Asimow and Langmuir*, 2003]. Furthermore, the shape of the melting regime influences the extent of melting and the resulting melt composition [*Forsyth*, 1993]. Geochemical melting models often assume a simple vertical column for partial melting in mid-ocean environments, but several authors have shown that melt may be focused from a 3-D region [e.g., *Sparks and Parmentier*, 1991] and models of the influence of melt compositions on melt regime shape have been developed for major and trace elements [*Plank and Langmuir*, 1992; *Kinzler*, 1997]. As such, we utilize the fractional melting model of *Kinzler and Grove* [1992b, 1992a, 1993], in which melting is a function of temperature, pressure, and mantle composition. The benefit of this method is that the model simultaneously tracks residual mantle and melt compositions, as well as extents of melting. Furthermore, the melting parameterization of *Kinzler and Grove* [1992a, 1992b, 1993] utilizes extensive experimental results that are tailored specifically to mid-ocean ridge basalts. We calculate aggregate melt compositions utilizing a shaped melting regime. Specifically, the extent of melting and resultant lava composition are predicted using a three-step process: (1) melt production and composition are calculated at each point in the melting region assuming polybaric, near-fractional melting; (2) melt migrates vertically until it reaches the shallowest point of the melt surface and pools; and (3) in the shallow mantle lithosphere, mantle cooling induces fractional crystallization of the pooled melt and lava composition is predicted.

2.2.1. Step 1: Fractional Melting

[12] The polybaric fractional melting model of Kinzler and Grove (hereafter "KG92") utilizes a parameterized solidus derived from experimental data to calculate extents of melting [*Kinzler and Grove*, 1992b, 1992a, 1993]. Specifically, the solidus temperature, T_s, is given by:

$$T_s = 1157 + 16*(p - 0.001) - 38.7*(1 - Mg\#)$$
$$- 181*(NaK\#) - 0*(TiO_2), \quad (9)$$

in the spinel stability field (pressure, $p \geq 9$ kbars) and by:

$$T_s = 1242 + 9*(p - 0.001) - 120*(1 - Mg\#) - 89*(NaK\#)$$
$$- 6.6*(TiO_2). \quad (10)$$

in the plagioclase stability field ($p < 9$ kbars). The oxides TiO_2, Na_2O, CaO, and K_2O are estimated with the nonmodal batch melting equation:

$$C_{i,m} = \frac{C_0}{(D_{i,s} + F(1 - P_{i,m}))}, \quad (11)$$

where $C_{i,m}$ is the concentration of oxide (i) in the melt (m), C_0 is the initial mantle concentration, $D_{i,s}$ is the bulk

Table 3. Estimated MORB Mantle Source Composition

	Mantle Compositions							
	SiO$_2$	TiO$_2$	Al$_2$O$_3$	FeO	MgO	CaO	K$_2$O	Na$_2$O
W&H DMM[a]	45.0769	0.1311	4.0926	8.2471	39.0478	3.196	0.006	0.2823

	Mantle Modes[b]							
	aug	opx	oliv	plag	aug	opx	oliv	spin
W&H DMM	0.128	0.261	0.546	0.065	0.13	0.28	0.57	0.02

[a]Bulk depleted MORB mantle composition of *Workman and Hart* [2005] (DMM) renormalized excluding Cr$_2$O$_3$, MnO, NiO, and P$_2$O$_5$.

[b]Aug, augite; opx, orthopyroxene; oliv, olivine; plag, plagioclase; spin, spinel.

partition coefficient of oxide (*i*) in the initial solid (*s*), $P_{i,m}$ is the bulk partition coefficient of the oxide in the melt, and *F* is the melt fraction. The oxide concentrations are calculated iteratively using a bisection method that systematically moves the endpoints of an initial "guess" interval closer together until they converge on a value where the error is minimized. MgO and FeO are also calculated iteratively by solving the mass balance equations:

$$[MgO]_b = [MgO]_m F_c - [MgO]_r (1 - F_c), \qquad (12)$$

$$[FeO]_b = [FeO]_m F_c - [FeO]_r (1 - F_c), \qquad (13)$$

where $[MgO]_b$ is the MgO of the initial bulk mantle composition, $[MgO]_m$ is the MgO of the melt, and $[MgO]_r$ is the MgO of the residual mantle (where the square brackets denote cation mole percent). Similarly, $[FeO]_b$ is the FeO of the initial mantle composition, $[FeO]_m$ is the FeO of the melt, and $[FeO]_r$ is the FeO of the residual mantle. In this formulation, F_c refers to the fraction of melt produced in cation fraction units (see *Kinzler and Grove* [1993] for further discussion). Once the oxides concentrations are determined using equations (11)–(13), the Mg #$_m$ and NaK #$_m$, the Mg and NaK numbers of the melt, are calculated as:

$$Mg\#_m = \frac{[MgO]_m}{[MgO]_m + [FeO]_m} \qquad (14)$$

$$NaK\#_m = \frac{(Na_2O + K_2O)}{(Na_2O + K_2O + CaO)} \qquad (15)$$

[13] It is widely accepted that the process of melt generation beneath a mid-ocean ridge spreading center is adia-

batic and occurs over a range of pressures [*Klein and Langmuir*, 1987]. Therefore, we utilize the polybaric incremental batch accumulated melting approach with incomplete melt withdrawal (model 3 in KG92) to approximate fractional melting of the mantle. This approach assumes a constant melt production rate of 1% melt per 1 kbar of ascent. At each melting increment, 99% of the generated melt is removed and accumulated elsewhere; the remaining melt and depleted mantle ascend another 1 kbar where they are further melted by 1% [*Ahern and Turcotte*, 1979]. As melting proceeds, the latent heat effect of the melting reaction acts to decrease the mantle temperature. We assume a constant latent heat and that the enthalpy of melting does not change over small extents of melting. We incorporate the change in temperature, ΔT, at each step in the calculation as a function of melt fraction, the latent heat of melting, L, and heat capacity, C_p, using the following formulation [*Turcotte*, 1982]:

$$\Delta T = \frac{F L}{C_p}. \qquad (16)$$

To determine the temperature structure input into the KG92 melting model, the mantle potential temperature, T_p, at the base of the model domain is set to a value between 1300°–1400°C. Note that, T_p is defined as the mantle temperature at the surface extracted along an adiabatic gradient of 0.5°C/km to depth.

[14] In the original KG92 model, pressure controls the cessation of melting and fractional melting is assumed to stop at 4 kbars at the top of a vertical melt column. In our implementation, melting begins when the adiabatic temperature profile crosses the solidus and continues until conductive cooling from the surface depresses the geotherm below the solidus. The shape of the melting regime is also estimated (see section 2.2.2). We assume that the mantle is described by a four-phase assemblage (olivine, clinopyroxene, orthopyroxene, and an aluminous phase, either spinel or plagioclase depending on the pressure, see Tables 3–5) and utilize the depleted MORB mantle (DMM) composition of *Workman and Hart* [2005] as the initial major element mantle composition of the mantle (Table 3).

2.2.2. Step 2: Melt Migration

[15] To calculate the final melt composition and the resultant crustal production, our model must determine how melt migrates from the melting region to a nearby spreading center. Previous 3-D melt migration models have proposed that melt percolating upward through the hot, permeable mantle will pool along a low permeability boundary (e.g., the top of the melting region, the base of the lithosphere, or the cpx-out reaction zone) and then

Table 4. Plagioclase-Lherzolite Melting[a]

	Distribution Coefficient[b]			
Oxide	Olivine	Orthopyroxene	Augite	Plagioclase
K$_2$O	0.001	0.001	0.001	0.27
Na$_2$O	0.001	0.04	0.15	1.0
TiO$_2$	0.03	0.2	0.41	0.001
CaO	0.03	–	–	1.32

[a]Pressures < 9 kbar.
[b]Distribution coefficients from *Kinzler and Grove* [1992a, Table A1].

Table 5. Spinel-Lherzolite Melting[a]

	Distribution Coefficient[b]			
Oxide	Olivine	Orthopyroxene	Augite	Spinel
K$_2$O	0.001	0.001	0.001	0.001
Na$_2$O	0.001	0.04	0.2	0.001
TiO$_2$	0.03	0.2	0.41	0.135
CaO	0.03	–	–	0.018

[a]Pressures ≥ 9 kbar.
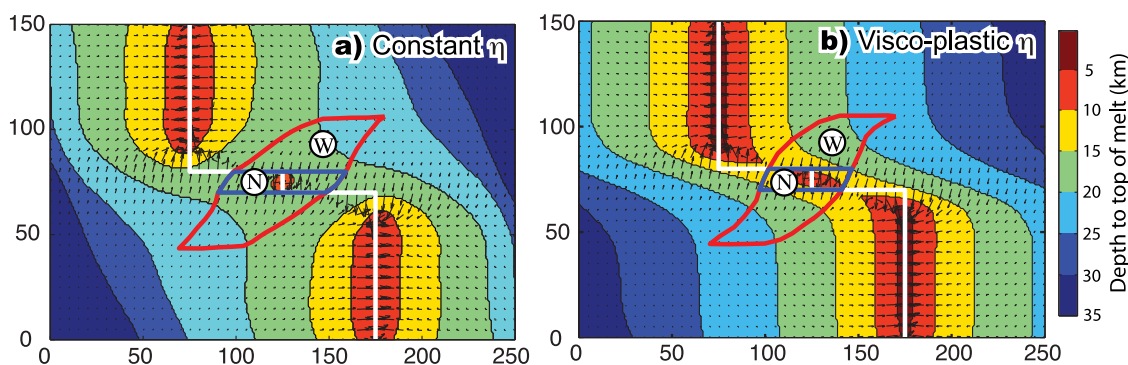[b]Distribution coefficients from *Kinzler and Grove* [1992a, Table A2].

Figure 4. Depth to the top of the melting region with chosen pooling areas for the (a) constant viscosity rheology and (b) viscoplastic rheology. Region W (delineated by red outline) delineates the wide melt pooling model, which pools the entire area of melts that have the potential to migrate toward the ITSC. In contrast, region N (outlined in blue) assumes that melts will not migrate across the transform fault to the ITSC. Black arrows indicate the gradient of the melt surface and the direction of melt migration. T_p = 1350°C and Nu = 4.

migrate laterally, "uphill," along this boundary to the ridge axis [*Sparks and Parmentier*, 1991; *Sparks et al.*, 1993; *Magde and Sparks*, 1997; *Magde et al.*, 1997; *Kelemen and Aharonov*, 1998]. To simulate this two-step melt migration process, we assume that melt first migrates vertically to the top of the melting region and then migrates laterally up the slope of the top of the melting region until it reaches a local minimum in the surface, which typically corresponds to a nearby spreading center. Melt migration patterns for the constant and viscoplastic mantle rheology models are shown for a 100-km-long transform fault bisected by a 10-km-long ITSC (Figure 4). The depth to the top of the melt surface is contoured and the gradient of the surface (black arrows) is plotted to indicate the slope of the melt surface and the direction the melt will migrate.

[16] Uncertainties with the melt migration model include (1) how far melt will migrate along this boundary before it freezes and (2) whether melt will be extracted vertically before it reaches the ridge axis or ITSC. To explore these processes, we investigate two end-member scenarios for melt migration beneath the transform fault domain. The first scenario assumes a wide pooling region in which all of the melt projected to migrate to the transform domain will aggregate at the ITSC (solid red lines in Figure 4). The capture area delineated by the solid red lines in Figure 4 is determined using the slope of the melt surface and calculating where the melt will migrate. The second end-member scenario assumes that melt is unlikely to migrate across a transform fault or fracture zone due to the increased fracture permeability within the fault zone; that is, the melt will use these more-permeable pathways created by the fault and not continue to the ITSC. In this case, melt that reaches the ITSC is only pooled from the narrow region of the mantle delineated between the two fault zones (solid blue lines in Figure 4). These models will be referred to as migration model 1, wide pooling region, and model 2, narrow pooling region, in all subsequent discussions.

[17] Crustal thickness at the ITSC is calculated by integrating the melt production rate over the entire pooling area that is tapped by the ITSC. The integrated melt production rate is then divided by the spreading rate and the length of the ITSC yielding an average crustal thickness for each ITSC [*Forsyth*, 1993].

2.2.3. Step 3: Fractional Crystallization

[18] Finally, to approximate fractional crystallization of the melt prior to eruption we use the approach of *Yang et al.* [1996]. This method assumes isobaric fractional crystallization and calculates the fractional crystallization path as a function of melt composition and pressure between 0.1 to 800 MPa (i.e., 1 bar to 8 kbars). In our models, crystallization pressure is constrained by the depth at which the melting ceases. *Yang et al.* [1996] uses algebraic relations obtained from experimentally determined phase boundaries for olivine-clinopyroxene-quartz and olivine-clinopyroxene-plagioclase in pseudoternary projections, and constraints from mineral-melt exchange reactions derived from experimentally produced mineral-melt pairs. This model provides major element composition for each step of fractional crystallization.

[19] The composition of the pooled melt is then used to determine the liquid line of decent (LLD) and to calculate proxies such as $Fe_{8.0}$ and $Na_{8.0}$, which can be compared to observed major element variations. The LLD represents the crystallization path that melt will take as it cools in the shallow parts of the mantle. Transitions in the crystallizing phase assemblage are illustrated by the kinks in the slopes of the lines, which in most cases represent the transitions from the equilibrium phases of olivine + melt, to olivine + plagioclase + melt, to olivine + plagioclase + clinopyroxene + melt. Fractionation corrected values of the oxides FeO and Na_2O are used as proxies for depth and extent of melting, respectively.

3. Numerical Modeling Results

3.1. Benchmark: Comparison to EPR 9°N

[20] To calibrate parameters such as T_p and the maximum horizontal distance for melt migration, W_{pool}, lava compositions are first calculated in 2-D and compared to observations of crustal thickness [*Canales et al.*, 2003] and lava composition [*Batiza and Niu*, 1992] at 9°N on the EPR. For a constant viscosity rheology, the crustal thickness calcu-
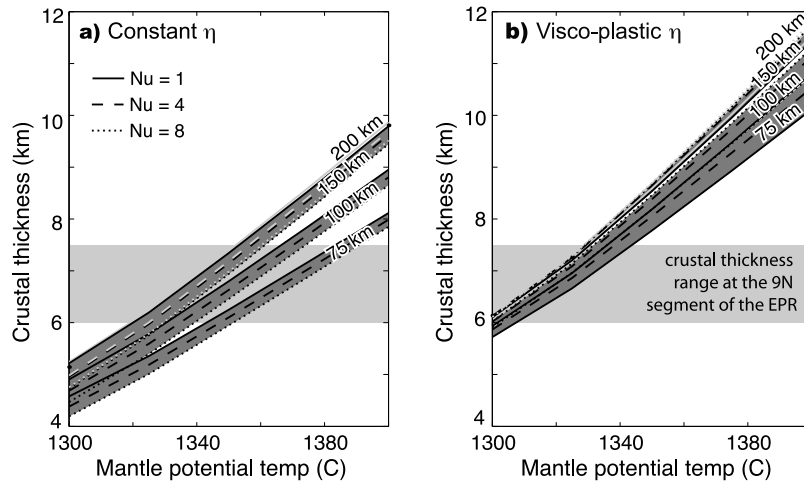
Figure 5. Comparison of the predicted crustal thickness at the ridge axis for various widths of the melt pooling regions (W_{pool} = 200, 150, 100, and 75 km) and hydrothermal cooling (Nu = 1, 4, and 8) for the (a) constant viscosity rheology and (b) viscoplastic rheology. The light gray shaded region indicates the seismic crustal thickness variations observed at the 9°N segment of the EPR [*Canales et al.*, 2003].

lated for T_p = 1325°C–1350°C correlates well with the seismic observations (Figure 5a). While pooling melt over a wider region results in greater crustal thickness, incorporating hydrothermal cooling (Nu = 4 and 8) decreases the predicted crustal thickness (Figure 5a). As discussed above, the viscoplastic rheology produces a warmer temperature structure beneath the ridge axis, resulting in thicker crust. We find that T_p = 1325°C best fits the seismic observations at EPR 9°N (Figure 5b). Incorporation of hydrothermal cooling with the viscoplastic rheology further focuses mantle upwelling beneath the ridge creating larger upwelling velocities and slightly thicker crust (Figure 5b).

[21] We also investigated the sensitivity of $Fe_{8.0}$ and $Na_{8.0}$ to T_p and W_{pool} (Figure 6). $Fe_{8.0}$ and $Na_{8.0}$ are normalizations of the wt % FeO and wt % Na_2O to 8 wt % MgO [*Klein and Langmuir*, 1987]. $Fe_{8.0}$, which is classically viewed as a proxy for the mean pressure of melting, increases as the pressure/depth of melting increases. Since Na is highly incompatible, $Na_{8.0}$ is generally used as a proxy for the extent of melting, decreasing as the extent of melting increases. As T_p increases the onset of melting occurs at greater depths, resulting in higher values of $Fe_{8.0}$ (Figure 6). Additionally, raising T_p increases the extent of melting and thus $Na_{8.0}$ is predicted to decrease (Figure 6).
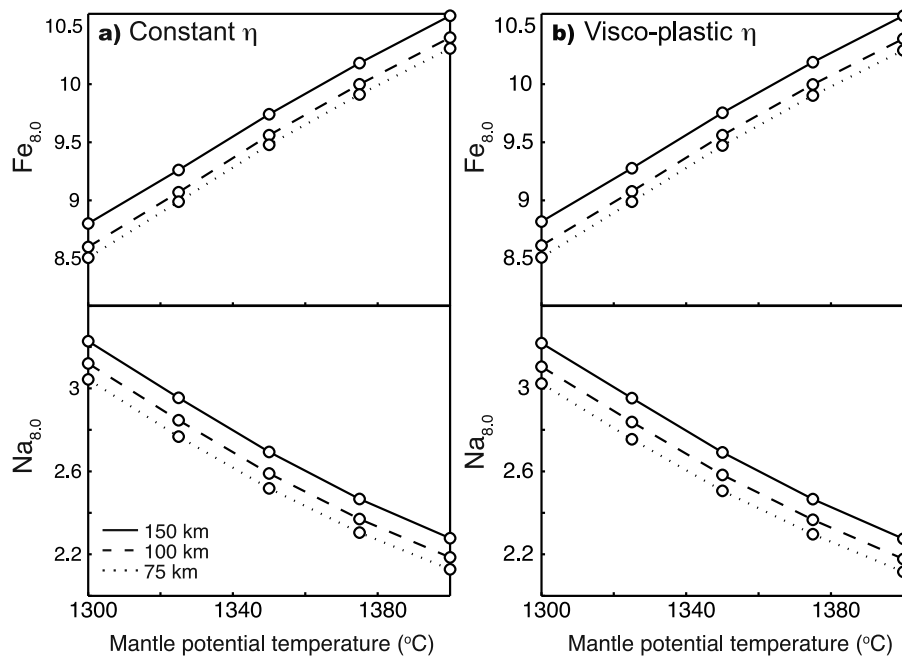

Figure 6. Calculated $Na_{8.0}$ and $Fe_{8.0}$ as a function of mantle potential temperature, T_p. Nu = 4 for models of W_{pool} = 75 km, 100 km, and 150 km. (a) Constant viscosity and (b) viscoplastic rheology. Open circles indicate values from individual model runs.
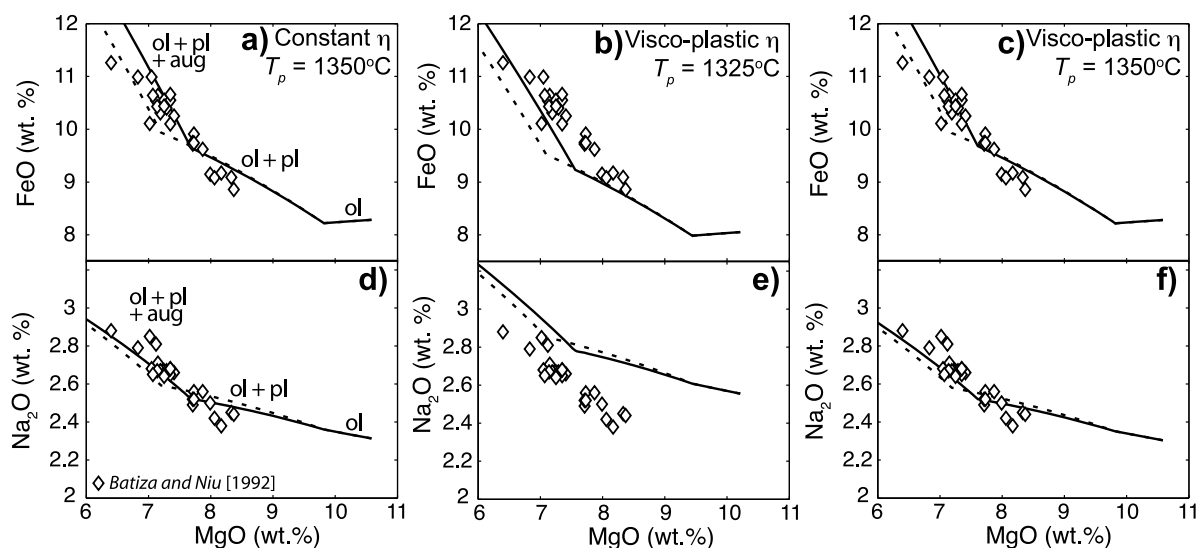
Figure 7. Calculated (a–c) FeO and (d–f) Na_2O versus MgO for 2-D models of a ridge with a half spreading rate of 50 mm/yr, W_{pool} = 75 km, and Nu = 4. Data points are from major element microprobe analyses of basalt glass samples collected along the 9°N segment of the EPR by *Batiza and Niu* [1992]. Crystallizing phases that correspond to changes in the LLD slope are noted in Figures 7a and 7d: ol, Olivine; pl, Plagioclase; aug, Augite. Figures 7a and 7d show the constant viscosity model with T_p = 1350°C. The solid black line indicates fractional crystallization at top of the melt column and the dashed line indicates crystallization at 0.2 kbar. Figures 7b and 7e show models for viscoplastic rheology with T_p = 1325°C. Figures 7c and 7f show models for viscoplastic rheology with T_p = 1350°C.

However, while $Fe_{8.0}$ and $Na_{8.0}$ are strongly dependent on T_p, they vary only slightly with mantle rheology and W_{pool}.

[22] To calibrate the values for T_p and W_{pool} used in our models, we compare our 2-D ridge results to the geochemical observations of *Batiza and Niu* [1992]. These data include major element compositions of basaltic glasses from a comprehensive dredging program at ∼9–10°N along the EPR and its flanks. We find that, T_p = 1350°C, Nu = 4, and W_{pool} = 75km results in a reasonably good fit to the observed FeO and Na_2O data (Figures 7a, 7c, 7d, and 7f). The pressure at the top of the melting triangle varies for each model run depending on T_p (solid black line in Figure 7). For T_p = 1350°C the top of the melting region is at 2.4 and 2.0 kbars for the constant viscosity model and the viscoplastic rheology models, respectively.

[23] For the viscoplastic rheology, T_p = 1325°C provides the best match to the seismically observed crustal thicknesses at the EPR 9°N (Figure 5). However, T_p = 1350°C better predicts the Na_2O and FeO values observed in microprobe analyses of glass samples from the EPR 9°N. There is also a discrepancy in the prediction of $Fe_{8.0}$ and $Na_{8.0}$. The *Batiza and Niu* [1992] data indicate an $Fe_{8.0}$ ∼ 9 and $Na_{8.0}$ ∼ 2.4, which corresponds to our model predictions for T_p = 1325°C and 1360°C, respectively, assuming W_{pool} = 75 km (Figure 6). Based on our 3-D model results, described later, we believe that these discrepancies arise from complexities in the pattern of melt migration, which controls crustal thickness variations, though we cannot rule out mantle heterogeneity. Because T_p = 1350°C provides the best match to the major element compositions and T_p = 1325°C best matches the crustal thickness data, we investigate 3-D models in later sections with both of these temperature constraints.

[24] We also compare the melt productivity predicted by KG92 with two other melt models, *Reid and Jackson* [1981] (hereinafter referred to as RJ81) and *Katz et al.* [2003] (hereinafter referred to as K03). RJ81 incorporates a pressure-temperature solidus relationship and calculates melting linearly as a function of the difference between the temperature of the mantle and of the solidus at a given pressure. K03 incorporates the *Hirschmann* [2000] solidus into a parameterized equation for mantle melting. KG92 differs from the melting approximations of the RJ81 and K03 models because its solidus is reached at shallower depths in the mantle [*Reid and Jackson*, 1981; *Katz et al.*, 2003]. As a result, the KG92 model produces lower extents of melting than do the K03 and RJ81 models, with mean extents of melting ranging from 5 to 6% for KG92 to 9–10% and 7–9% for RJ81 and K03, respectively. These differences become important when estimating production of crust and the predicted lava composition. To match the crustal thicknesses observed at the EPR 9°N segment, the RJ81 and K03 models require much shorter distances of melt migration to the ridge axis and/or lower values of T_p compared to KG92.

3.2. Results of 3-D Segmented Transform Fault Results

[25] We investigate the effects of fault segmentation on melt production and migration by exploring a series of models with different ITSC lengths (Figure 2). Using the parameters from the 2-D models that best fit the EPR 9°N data, we assume T_p = 1350°C, Nu = 4, and U_0 of 50 mm/yr for the constant viscosity models and T_p = 1325°C and 1350°C for the viscoplastic rheology models. Similar to the 2-D results, for a specific value of T_p the principal factor controlling crustal thickness is the volume of mantle over
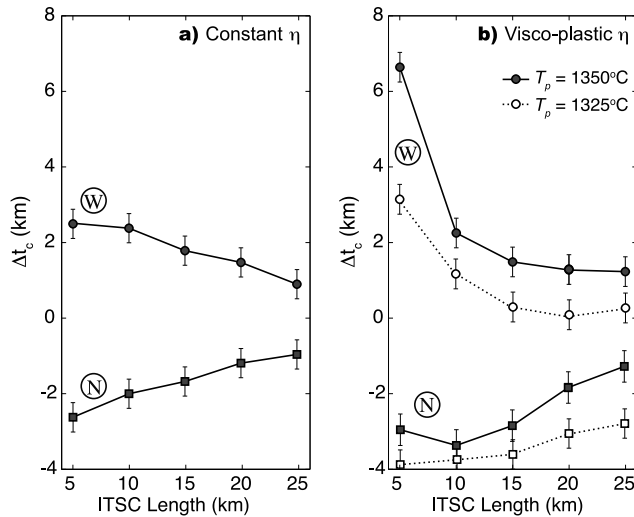
Figure 8. Calculated change in crustal thickness, Δt_c, as a function of L_{ITSC}, where Δt_c is defined as the difference between the predicted 3-D crustal thickness at the ITSC and a reference model assuming 6 km of crust. Calculations were done for the (a) constant viscosity and (b) viscoplastic rheology. Model W incorporates melt from the wide pooling region (circle symbols), while model N is for the narrow melt pooling region model (square symbols). Each symbol is the result of a single 3-D model run. Top and bottom error bars indicate the range in the calculated crustal thickness by using the melt surface contour of 0.05 and 0.1, respectively. Calculations with $T_p = 1350°C$ and Nu = 4 are indicated by filled symbols, whereas models with $T_p = 1325°C$ and Nu = 4 are indicated by open symbols.

which melt is pooled (Figure 8). This is illustrated by investigating the change in crustal thickness, Δt_c, at the ITSC as compared to a reference crustal thickness of 6 km. For the wide melt pooling (model 1) we find that as L_{ITSC} increases, Δt_c decreases (Figure 8). This is because, for $L_{ITSC} < 25$ km, ITSCs pool melt from a similar sized mantle region. Hence, when the pooled melt is averaged over the length of the ITSC, there is a larger effect on predicted crustal thickness for shorter ITSCs. As the length of the ITSC increases, it behaves more like a steady state 2-D ridge segment. For narrow pooling (model 2) as the ITSC length is increased, the predicted crustal thickness increases (Figure 8). Compared to calculations with a constant viscosity, the viscoplastic rheology model promotes focused upwelling in regions of increased strain rate beneath the transform and thus systematically predicts greater variations in crustal accretion relative to the adjacent ridge segments.

[26] Fault segmentation also influences melt composition at the ITSCs. For both wide and narrow melt pooling models, calculations with a constant viscosity predict both $Fe_{8.0}$ and $Na_{8.0}$ to decrease as the length of the ITSC increases (Figure 9a). These trends suggest that the extent of melting increases and the average pressure of melting decreases as the L_{ITSC} increases. This is consistent with the predicted mantle thermal structure, because increasing the length of the ITCS will eventually create a warmer ridge segment with higher extents of melting and melting to shallower depths.

[27] In contrast, cases with a viscoplastic rheology predict relatively uniform lava composition within the transform fault domain (Figure 9b). This occurs because the viscoplastic rheology produces an overall warmer thermal structure at the ITSC, which is relatively insensitive to the length of the ITSC. This indicates that the compositional signature of the transform fault is sensitive to mantle rheology. Specifically, models with a constant viscosity predict a greater transform fault effect on ITSC lava chemistry.

4. Applications to the Siqueiros Transform Fault System

4.1. Tectonic Setting

[28] The Siqueiros transform fault (Figure 1b) has been the site of several investigations including rock dredging and Alvin dives [*Perfit et al.*, 1996], magnetic [*Carbotte and Macdonald*, 1992] and gravity [*Gregg et al.*, 2007] studies, and detailed geologic mapping [*Fornari et al.*, 1989]. This wealth of data makes it an ideal location to investigate the effects of fault segmentation on melting and melt extraction. The Siqueiros transform system is a ~140-km-long, left-stepping offset located between 8° 20N and 8° 30N on the EPR. The half slip rate of the transform system is ~55 mm/yr [*DeMets et al.*, 1990, 1994]. Bathymetry and side-scan sonar collected from Siqueiros reveal that the transform system is segmented into five fault strands separated by four ITSCs labeled A–D from west to east (Figure 10) [*Fornari et al.*, 1989]. The current, segmented geometry of Siqueiros transform is thought to be the result of several discrete periods of counterclockwise rotation in the spreading direction (~4–8°) over the past 3 Myr [*Pockalny et al.*, 1997].

[29] Residual mantle Bouguer gravity anomalies calculated along the Siqueiros transform fault system suggest a mass deficit within the transform fault domain [*Gregg et al.*, 2007]. Assuming that the entire gravity anomaly is due to crustal thickness variations, the gravity data indicate excess crustal thickness (as compared to a reference crust of 6 km) of up to 1.5 km associated with the bathymetric high of ITSC D (Figure 2c). Excess crust is also associated with ITSCs B and C along the central portion of the transform fault as well as in the inactive fracture zones on either side of the Siqueiros transform system [*Gregg et al.*, 2007]. Gravity analysis did not reveal excess crust at ITSC A.

[30] We incorporate the geometry of Siqueiros transform system into a 3-D model to evaluate melting and melt migration beneath the fault zone. ITSCs A–D range in length from 10 km at ITSC A to <5 km at ITSC D. Due to the obliquity of the ITSCs within the transform fault and the computational difficulty of the exact geometry, the orientations of the ITSCs have been modified to be orthogonal to the transform fault and parallel to the adjacent ridge segments (Figure 11).

4.2. Crustal Thickness Predictions at Siqueiros

[31] We find that model-predicted crustal thickness variations at the Siqueiros fault system are strongly dependent on mantle rheology (Figure 11). The constant viscosity rheology predicts a cooler mantle beneath the transform system and, subsequently, lower extents of melting compared to the viscoplastic rheology. Along the western
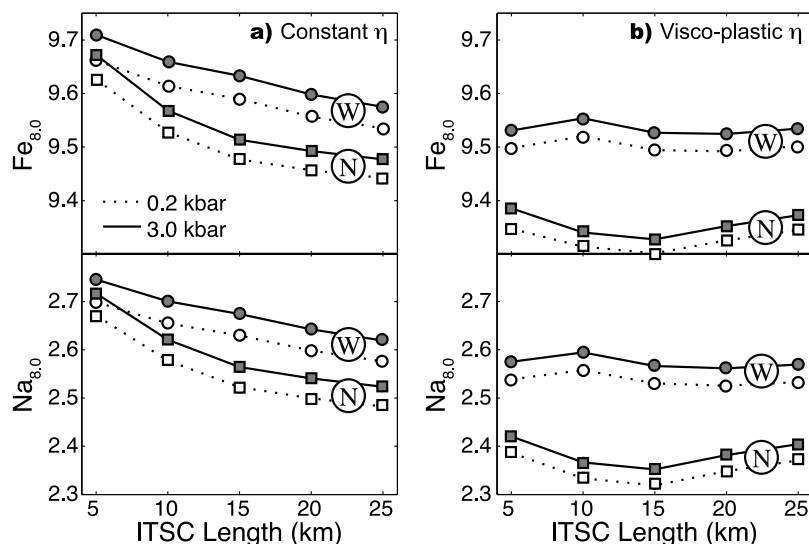
Figure 9. Calculated $Fe_{8.0}$ and $Na_{8.0}$ as a function of L_{ITSC} for the (a) constant viscosity rheology and (b) viscoplastic rheology. Model W is for wide melt pooling region, while model N is for narrow melt pooling region. Gray circles on solid lines indicate calculations for fractional crystallization at 3.0 kbar. Open circles on dotted lines indicate calculations for fractional crystallization at 0.2 kbar. Each symbol represents the result of a single model run. $T_p = 1350°C$ and $Nu = 4$.

portion of Siqueiros, the predicted crustal thickness variations from the wide melt pooling model (model 1) with a constant viscosity mantle match the gravity-derived crustal thicknesses calculated for ITSCs A and B (Figure 11c). However, the predicted crustal thicknesses diminish to the east and are a poor fit to the gravity-derived crustal thicknesses at ITSCs C and D. In contrast, a wide pooling model with viscoplastic rheology provides a good fit to the gravity-derived crustal thickness data at all four ITSCs (Figure 11d).

[32] The key difference between the viscoplastic and constant viscosity models is that the viscoplastic rheology predicts a warmer shallow mantle directly beneath the transform fault domain and deeper melting near the transform, resulting in higher overall extents of melting. The warmer temperature structure causes each ITSC to produce a local minimum in the melt surface thereby focusing melt extraction and enhancing crustal accretion (Figure 11b). Finally, the crustal thickness values predicted using narrow melt pooling (model 2) for both the constant and viscoplastic rheologies are significantly smaller than those derived from residual mantle Bouguer gravity data, indicating that a wide melt pooling region is necessary to produce the crustal thickness variations estimated from the gravity data.

4.3. Geochemical Predictions at Siqueiros

[33] We next compare the model-predicted liquid lines of descent (LLD) to major element analyses of the glassy chill margins from fresh basalts collected via dredge and Alvin dive along the Siqueiros fault system (Figure 10) [*Perfit et al.*, 1996; *Hays*, 2004]. The maximum pressure at which fractional crystallization can begin corresponds to the depth where melting ceases (solid lines in Figures 12 and 13). We also show a fractional crystallization model for 0.2 kbars, corresponding to the average seafloor depth (dashed lines in Figures 12 and 13).

[34] The constant and viscoplastic rheology models compare favorably to the observed FeO composition and there is

very little difference between the wide and narrow pooling models. The warmer temperatures resulting from the viscoplastic rheology model produce slightly lower FeO implying lower average pressures of melting compared to the constant viscosity rheology (Figures 12a–12d). However, for all models, fractional crystallization beginning at the depth of melt termination (solid LLD in Figures 12 and 13) fits the data better than fractional crystallization at shallower depths (dashed LLD in Figures 12 and 13). The kinks in the slope of the model calculated LLD change at a different values of MgO than is seen in the data, which may indicate that crystallization is polybaric (Figures 12c and 12d). As such, incorporating polybaric fractional crystallization in future models may help to better match the trend observed in the FeO data.

[35] Na_2O data from the Siqueiros ITSCs and transform segments are highly variable spanning a range of 2.2–2.9 wt % (Figure 13). While the viscoplastic rheology with wide melt pooling predicts compositions that are in the middle of the observed range, a single model does not fully predict the full range of values (Figures 13c and 13d).
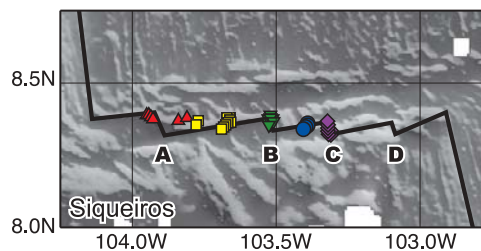

Figure 10. Shaded bathymetry for the Siqueiros Transform showing the locations of rock dredge and Alvin dive samples (colored symbols) collected along the transform fault [*Hays*, 2004]. The solid black line indicates the plate boundary, while the letters denote individual ITSCs.
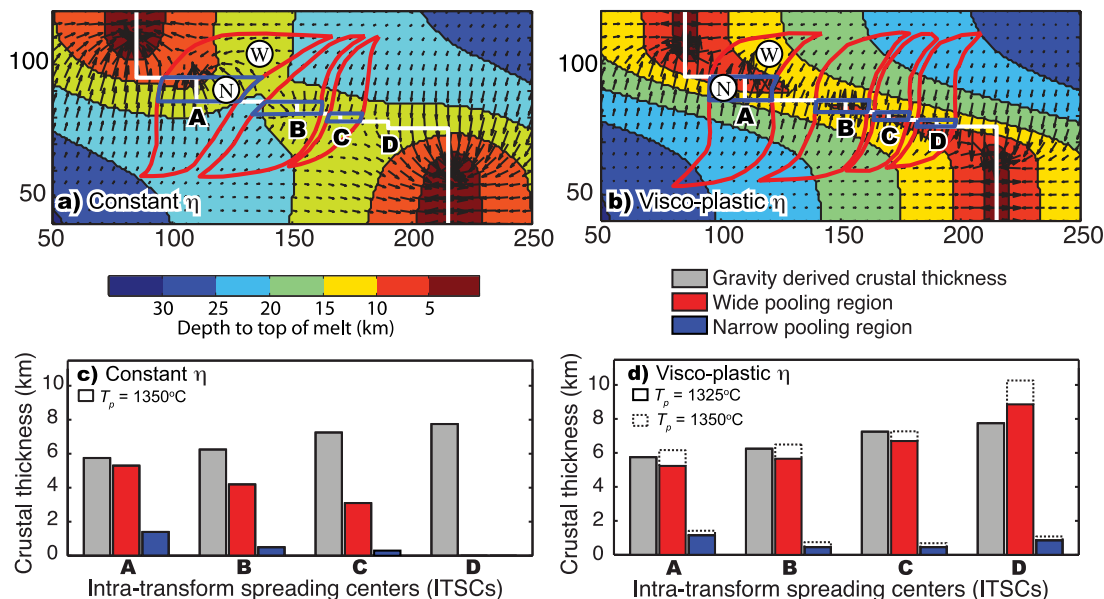
Figure 11. Results from the Siqueiros Transform melting models. (a) Depth to the top of melting calculated for a ridge-transform-ridge system with the geometry of Siqueiros and a constant viscosity. Arrows indicate the local spatial derivative of the melt surface that is assumed to be the melt migration direction. Red solid lines indicate wide melt pooling regions (W). Blue solid lines indicate the narrow melt pooling regions (N), which assumes that melt does not migrate across the transform fault. (b) Depth to the top of the melt surface for the viscoplastic rheology case. (c) Calculated and estimated crustal thickness values for the constant viscosity model. $T_p = 1350°C$ and Nu = 4. Gray bars show the gravity-derived crustal thicknesses at the Siqueiros transform fault from *Gregg et al.* [2007]. Red bars indicate the predicted crustal thickness for the wide pooling region model. Blue bars indicate the predicted crustal thicknesses for the narrow pooling region model. Note that no crustal accretion is predicted at spreading center D, as it is not a local minimum in the melt surface. (d) Crustal thickness predictions for the viscoplastic rheology. $T_p = 1325°C$ and Nu = 4. Note that this model does a much better job of predicting the crustal thicknesses as observed from the gravity calculations. Crustal thickness predictions for $T_p = 1350°C$ are indicated by the dotted lines.

Pooling melt from a narrow region of the mantle within the transform fault domain may explain some of the lower values of Na_2O values seen in particular at ITSC A, which is regarded as a long-lived ITSC [*Fornari et al.*, 1989]. On the other hand, utilizing a lower T_p of 1325°C results in melting at shallower depths and lower extents of melting, which may explain the higher Na_2O values observed at ITSC C and the transform segment between ITSCs B and C. The constant viscosity model underpredicts the extent of melting, i.e., Na_2O values that are too high, for both wide and narrow pooling (Figures 13a and 13b). This is consistent with the underprediction of crustal thickness using the constant viscosity model. In summary, the viscoplastic rheology with wide pooling and $T_p = 1350°C$ does the best job of fitting both the gravity-inferred crustal thickness data as well as the majority of the geochemical data (Figures 12 and 13).

5. Discussion

5.1. Factors Controlling Crustal Thickness Variations

[36] In General, melt migration beneath mid-ocean ridge spreading centers is poorly constrained. In 2-D ridge models, the predicted crustal thickness variations are primarily sensitive to W_{pool}, T_p, and the assumed melting model. For example, for $U_0 = 50$ mm/yr, $W_{pool} = 75$ km, and $T_p = 1350°C$, the KG92 melt model predicts a crustal thickness of 6–7 km, while the K03 and RJ81 melting models predict thicker crust on the order of 8–10 km. Therefore, to match the crustal thickness variations observed at the EPR 9°N segment, the RJ81 and K03 models require the migration of melt over shorter distances to the ridge axis or lower values for T_p.

[37] A similar relationship is observed in 3-D at ITSCs within a transform fault system. Previous studies have assumed that melts extruded at ITSCs came from directly below the transform fault domain or from the nearby ridge axis [*Fornari et al.*, 1989; *Hekinian et al.*, 1992, 1995; *Perfit et al.*, 1996; *Wendt et al.*, 1999], and have not discussed the possibility that melts may be drawn in across the transform fault from a large volume of the surrounding mantle. If we assume that the negative residual mantle Bouguer gravity anomaly observed along the Siqueiros fault system is primarily due to crustal thickness variations [*Gregg et al.*, 2007], our calculations show that melts must focus into the transform fault from a large volume of the mantle. The wide pooling model for the Siqueiros transform predicts that melts travel, on average, ~40 km to reach an
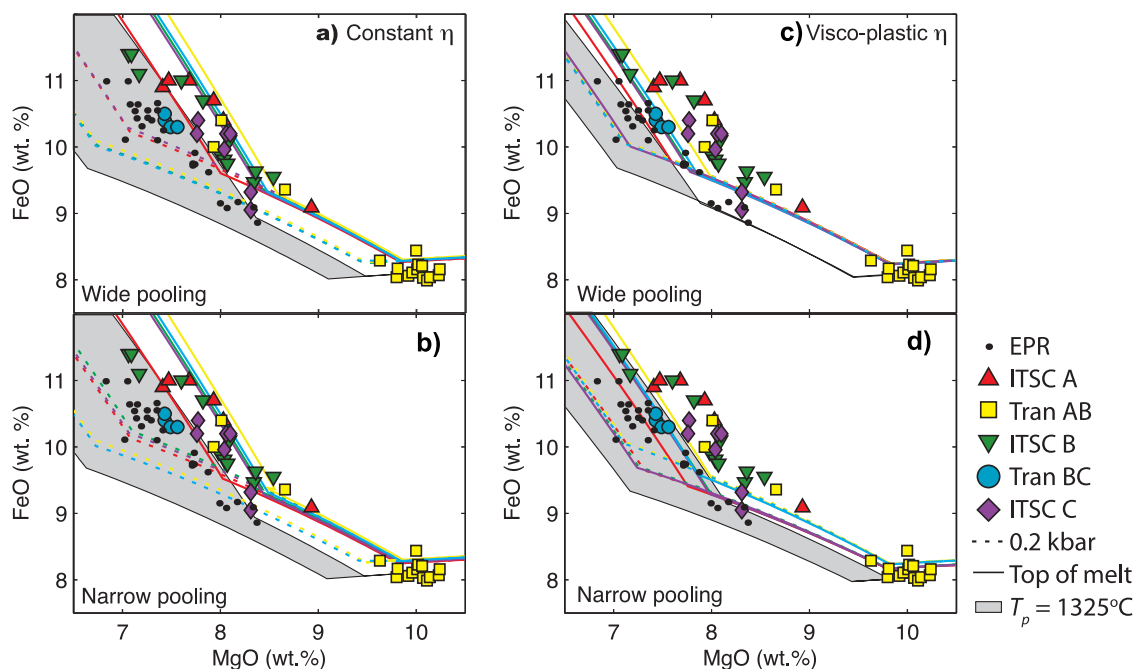
Figure 12. Liquid lines of decent (LLD) model calculations of FeO versus MgO. Colored LLD in each plot correspond to the color of the data point for each ITSC or transform fault strand as shown in the legend on the bottom right and in Figure 10. Solid LLD lines indicate fractional crystallization at the top of the melt surface, which ranges in depth from 18 to 24 km (6–8 kbar) for constant viscosity and 9–15.5 km (3–5 kbar) for viscoplastic rheology, while dashed LLD lines indicate fractional crystallization at 0.2 kbar, which would be expected for fractional crystallization in a shallow magma lens. All models were run for $T_p = 1350°C$ and Nu = 4. The gray shaded regions indicate the predicted model region for $T_p = 1325°C$. Models were run for (a and b) constant viscosity and (c and d) viscoplastic rheology and for a wide melt pooling region (Figures 12a and 12c) and a narrow melt pooling region (Figures 12b and 12d).

ITSC. This is approximately half the distance that melts are required to migrate (75 km) in our 2-D melting models to match the EPR 9°N data. However, since there are fresh lava flows observed along the fault strands separating the ITSCs, it is clear that some of the melt does not make it to the spreading segments [*Perfit et al.*, 1996]. Overall, we conclude that to generate enhanced crustal thicknesses within fast slipping transform systems by deep melt migration, melt must migrate into the transform domain from a wide region of underlying mantle.

[38] Gravity derived crustal thickness variations at the Garrett transform fault [*Gregg et al.*, 2007] also suggest that melt is tapped from a wide region of the mantle. The Garrett transform is ∼130 km long with three ITSCs containing four ridges of ∼9 km long that lie in between four fault strands [*Hekinian et al.*, 1992]. Peridotites collected from the Garrett transform are very depleted, indicating high degrees of melting in the mantle regions surrounding the fault system [*Niu and Hekinian*, 1997a, 1997b; *Constantin*, 1999]. However, the melt generated in the mantle surrounding the Garrett transform does not appear to migrate directly into the transform fault and aggregate at the ITSCs. Rather, the majority of the excess crust observed at the Garrett system is associated with the high topography flanking the transform fault and fracture zones and not with the ITSCs, which have crustal thicknesses equal to or less than the adjacent ridge segments [*Gregg et al.*, 2007]. These observations suggest that the melts pooled from a wide mantle

region surrounding the Garrett system are extruded on the flanks of the transform fault where more permeable pathways may have been produced by brittle deformation.

5.2. Effect of Siqueiros Transform on Mantle Melting

[39] The geochemical transform fault effect suggests that a cooler mantle region surrounding a transform fault system will promote deeper and lower extents of melting [*Bender et al.*, 1978, 1984; *Langmuir and Bender*, 1984; *Langmuir et al.*, 1986; *Reynolds et al.*, 1992; *Reynolds and Langmuir*, 1997]. This effect can be observed by comparing the major element compositions of lavas collected along the EPR 9°N segment and the Siqueiros transform fault system [*Batiza and Niu*, 1992; *Perfit et al.*, 1996; *Hays*, 2004] using the $Fe_{8.0}$ and $Na_{8.0}$ variables. Lavas from the EPR 9°N ridge segment have lower values of $Fe_{8.0}$ (∼9 wt % FeO, Figures 7 and 12), indicating a shallower mean pressure of polybaric melting. At the Siqueiros transform fault, erupted lavas have significantly higher values of $Fe_{8.0}$ (∼10–11 wt % FeO, Figure 12), indicating that the mean pressure of melting is deeper. This trend is also observed in the predicted compositions from our models. Thus, the transform fault effect noted by *Langmuir and Bender* [1984] is present in some major elements and is recoverable in our models.

[40] As described above, the incorporation of the viscoplastic mantle rheology creates a warmer thermal structure beneath the transform fault domain and subsequently lower pressures of melt cessation. This effect, coupled with
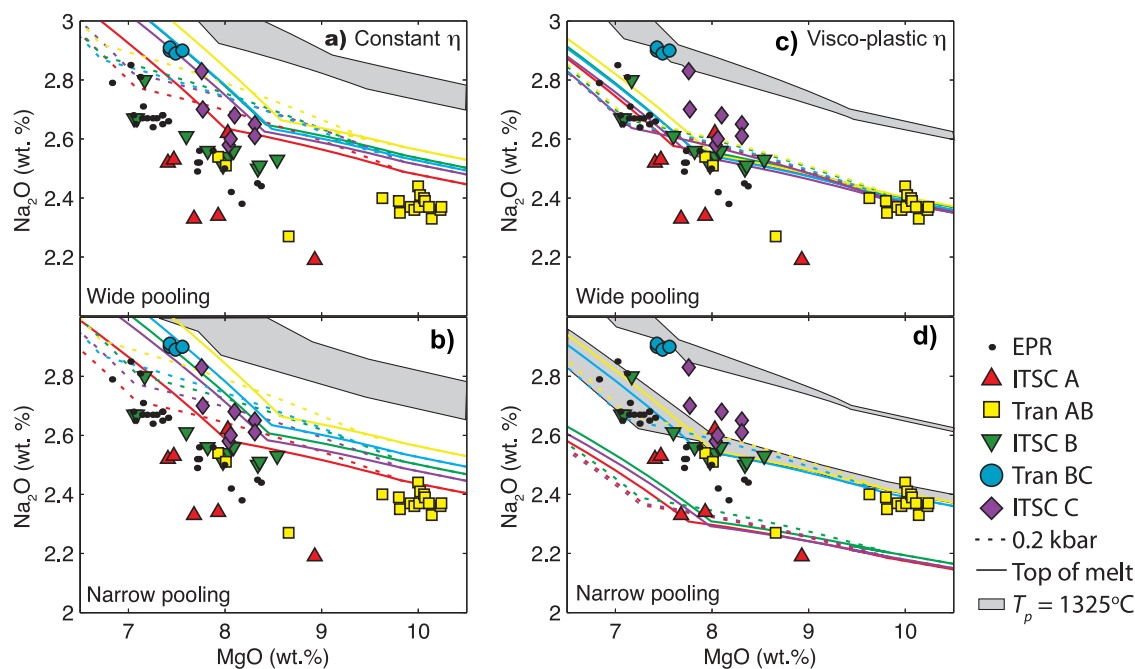
Figure 13. Liquid lines of decent (LLD) model calculations of Na_2O versus MgO. Colored LLD in each plot correspond to color of the data point for each ITSC or transform fault strand as shown in the legend on the bottom right and in Figure 10. Solid LLD lines indicate fractional crystallization at the top of the melt surface, which ranges in depth from 18 to 24 km ($6-8$ kbar) for constant viscosity and $9-15.5$ km ($3-5$ kbar) for viscoplastic rheology, while dashed LLD lines indicate fractional crystallization at 0.2 kbar, which would be expected for fractional crystallization in a shallow magma lens. All models were run for $T_p = 1350°C$ and Nu = 4. The gray shaded regions indicate the model region for $T_p = 1325°C$. Models were run for (a and b) constant viscosity and (c and d) viscoplastic rheology for a wide melt pooling region (Figures 13a and 13c) and a narrow melt pooling region (Figures 13b and 13d). The two gray shaded regions in Figure 13d indicate the regions obtained for $T_p = 1325°C$ and arise from the two clusters observed in the LLDs.

focusing melt from a large volume of the mantle around the transform fault, results in predicted crustal thicknesses at the ITSCs that are comparable to those observed at a 2-D ridge segment. Therefore, not only does the viscoplastic rheology model match the geophysical and geochemical observations at Siqueiros, this rheology does a very good job of explaining why the ITSCs of Siqueiros are producing volumes of lava equivalent to those produced at the EPR while simultaneously predicting deeper, lower extents of melting.

5.3. High-Pressure Fractional Crystallization

[41] While high-pressure fractional crystallization has been proposed in previous studies [*Michael and Cornell*, 1998; *Herzberg*, 2004; *Eason and Sinton*, 2006] to explain compositional variability at ridges with low magma flux, *Langmuir et al.* [1992] maintain that there are many problems associated with this mechanism. *Langmuir et al.* [1992] assert that in a ridge setting the lithosphere must be sufficiently thick to shut melting off at depth and for high-pressure crystallization to be predicted it must be consistent with melting processes. By combining fractional melting and crystallization models with mantle thermal models we are able to quantify both the termination of melting and the onset of crystallization and we illustrate that high-pressure fractional crystallization may occur in regions with thicker lithosphere such as beneath transform faults. At the 9°N segment of the EPR our models predict fractional

crystallization depths of $\sim 0-3$ km ($0.2-1.0$ kbar). These predictions are consistent with previous estimations for shallow crystallization beneath the EPR ridge axis [e.g., *Michael and Cornell*, 1998], while matching observed major element compositions [*Batiza and Niu*, 1992] and crustal thickness variations [*Canales et al.*, 2003]. On the other hand, we find that models with fractional crystallization at greater depths, $9-18$ km ($3-6$ kbars), fit the observed variations in composition at the Siqueiros transform fault ITSCs [*Perfit et al.*, 1996; *Hays*, 2004]. In fact, models of shallow crystallization do a very poor job of predicting the observed major element variations at the Siqueiros transform fault. Specifically, if shallow level fractional crystallization were occurring we would expect the observed compositions to fall upon the 0.2 kbar line in Figures 12 and 13. Since our models take into account the full melting process and begin crystallization at depths above melt termination, they are self-consistent given the physical constraints of melting and crystallization processes.

5.4. Melt Extraction at Siqueiros Transform Fault

[42] The observed major and trace element data from the Siqueiros transform system vary widely from enriched mid-ocean ridge basalt (EMORB) to depleted mid-ocean ridge basalt (DMORB). However, lavas from a single tectonic region within Siqueiros are relatively homogenous (e.g., Figure 13) [*Perfit et al.*, 1996; *Hays et al.*, 2004]. These

findings have led previous researchers to suggest that there are multiple mantle sources beneath the transform fault and that each ITSC and fault strand is independent of its neighbor and taps a different melt lens and/or mantle supply [*Fornari et al.*, 1989; *Perfit et al.*, 1996; *Hays*, 2004]. These models implicitly assume that the melt feeding into the transform domain must either come from directly below the transform fault or from the nearby ridge axis. In contrast, our 3-D thermal and melt models for Siqueiros indicate that the mantle flanking the transform fault supplies melt to the ITSCs. Specifically, by inferring the volume of the melting regime using the melt migration techniques of *Sparks and Parmentier* [1991] and then fractionally crystallizing the pooled melts at the depth of melt termination, we can reproduce the observed range in FeO and Na_2O (Figures 12c, 12d, 13c, and 13d).

[43] The higher $Fe_{8.0}$ values observed in the melts erupted at the ITSCs are likely a consequence of the large volume of deep mantle melts which are generated in the mantle adjacent to the transform fault and contribute to the pooled melts feeding the ITSCs. High-pressure fractional crystallization beneath the transform fault leads to earlier enrichment in FeO, which will further contribute to high $Fe_{8.0}$ values. The results of our models indicate that the majority of melts extracted at Siqueiros are aggregated from a large volume of mantle weighted toward deeper low-extent melts and the pooled melt collected from this volume experiences fractional crystallization at depths ranging from ∼9–18 km. This suggests that the variations in the composition of lavas from Siqueiros transform fault can be explained by the complexities of migrating melt into the transform fault, and the thermal effect of cold lithosphere in the fracture zone.

6. Conclusions

[44] Our investigation of melting, fractional crystallization, and melt extraction at segmented oceanic transform faults illustrates that, to explain the gravity-derived crustal thickness data from fast and intermediate slipping transforms, melt migration from a wide region of the mantle surrounding the transform fault is required. Significantly, these pooled melts contain a higher proportion of deep near-fractional melts that collect and erupt in the transform fault environment. We find that, depending on the length of an ITSC, crustal thickness at ITSCs is enhanced by 2–3 km for models incorporating an isoviscous rheology and up to 3–6.5 km for a temperature-dependent viscoplastic rheology. To match the gravity-derived crustal thickness variations observed within the Siqueiros transform fault (>1.5 km), melt must aggregate from a wide pooling area that extends up to 40 km on either side of the transform.

[45] Our model produces a geochemical transform fault effect of low extents of melting by pooling melts from a large volume of the mantle around the transform where melting shuts off at greater depths compared to beneath the adjacent ridge axes. This leads to increased crustal production in the transform while simultaneously producing pooled aggregate near-fractional melt compositions that are dominated by low-extent, deep melts. Finally, utilizing a temperature-dependent viscoplastic rheology, with $T_p = 1350°C$, in conjunction with the fractional melting model of *Kinzler and Grove* [1992a, 1992b, 1993] and the fractional

crystallization model of *Yang et al.* [1996], we demonstrate that the observed variations in major element composition from the Siqueiros transform fault can be explained by pooling melts from a wide region of the mantle and fractionally crystallizing them at the depth of melt termination.

References

Ahern, J. L., and D. L. Turcotte (1979), Magma migration beneath and ocean ridge, *Earth Planet. Sci. Lett.*, *45*, 115–122, doi:10.1016/0012-821X(79)90113-4.

Asimow, P. D., and C. H. Langmuir (2003), The importance of water to oceanic mantle melting regimes, *Nature*, *421*, 815–820, doi:10.1038/nature01429.

Baker, E. T., Y. J. Chen, and J. Phipps Morgan (1996), The relationship between near-axis hydrothermal cooling and the spreading rate of mid-ocean ridges, *Earth Planet. Sci. Lett.*, *142*, 137–145, doi:10.1016/0012-821X(96)00097-0.

Batiza, R., and Y. L. Niu (1992), Petrology and magma chamber processes at the East Pacific Rise similar to 9°30′N, *J. Geophys. Res.*, *97*, 6779–6797, doi:10.1029/92JB00172.

Behn, M. D., M. S. Boettcher, and G. Hirth (2007), Thermal structure of oceanic transform faults, *Geology*, *35*, 307–310, doi:10.1130/G23112A.1.

Bender, J. F., F. N. Hodges, and A. E. Bence (1978), Petrogenesis of basalts from project Famous Area—Experimental-study from 0-kbar to 15-kbars, *Earth Planet. Sci. Lett.*, *41*, 277–302, doi:10.1016/0012-821X(78)90184-X.

Bender, J. F., C. H. Langmuir, and G. N. Hanson (1984), Petrogenesis of basalt glasses from the Tamayo region, East Pacific Rise, *J. Petrol.*, *25*, 213–254.

Canales, J. P., R. S. Detrick, J. Lin, J. A. Collins, and D. R. Toomey (2000), Crustal and upper mantle seismic structure beneath the rift mountains and across a nontransform offset at the Mid-Atlantic Ridge (35°N), *J. Geophys. Res.*, *105*, 2699–2719, doi:10.1029/1999JB900379.

Canales, J. P., R. Detrick, D. R. Toomey, and S. D. Wilcock (2003), Segment-scale variations in the crustal structure of 150–300 kyr old fast spreading oceanic crust (East Pacific Rise, 8°15′N–10°5′N) from wide-angle seismic refraction profiles, *Geophys. J. Int.*, *152*, 766–794, doi:10.1046/j.1365-246X.2003.01885.x.

Carbotte, S., and K. Macdonald (1992), East Pacific Rise 8°–10°30′N—Evolution of ridge segments and discontinuities from Seamarc II and 3-dimensional magnetic studies, *J. Geophys. Res.*, *97*, 6959–6982, doi:10.1029/91JB03065.

Chen, Y. J., and W. J. Morgan (1990), A nonlinear rheology model for mid-ocean ridge axis topography, *J. Geophys. Res.*, *95*, 17,583–17,604, doi:10.1029/JB095iB11p17583.

Constantin, M. (1999), Gabbroic intrusions and magmatic metasomatism in harzburgites from the Garrett transform fault: Implications for the nature of the mantle-crust transition at fast-spreading ridges, *Contrib. Mineral. Petrol.*, *136*, 111–130, doi:10.1007/s004100050527.

DeMets, C., R. G. Gordon, D. F. Argus, and S. Stein (1990), Current plate motions, *Geophys. J. Int.*, *101*, 425–478, doi:10.1111/j.1365-246X.1990.tb06579.x.

DeMets, C., R. G. Gordon, D. F. Argus, and S. Stein (1994), Effect of recent revisions to the geomagnetic reversal time-scale on estimates of current plate motions, *Geophys. Res. Lett.*, *21*, 2191–2194, doi:10.1029/94GL02118.

Detrick, R. S., H. D. Needham, and V. Renard (1995), Gravity-anomalies and crustal thickness variations along the Mid-Atlantic Ridge between 33°N and 40°N, *J. Geophys. Res.*, *100*, 3767–3787, doi:10.1029/94JB02649.

Eason, D., and J. Sinton (2006), Origin of high-Al N-MORB by fractional crystallization in the upper mantle beneath the Galápagos Spreading Center, *Earth Planet. Sci. Lett.*, *252*, 423–436, doi:10.1016/j.epsl.2006.09.048.

Escartin, J., and J. Lin (1995), Ridge offsets, normal faulting, and gravity anomalies of slow spreading ridges, *J. Geophys. Res.*, *100*, 6163–6177, doi:10.1029/94JB03267.

Fornari, D. J., D. G. Gallo, M. H. Edwards, J. A. Madsen, M. R. Perfit, and A. N. Shor (1989), Structure and topography of the Siqueiros transform-fault system—Evidence for the development of intra-transform spreading centers, *Mar. Geophys. Res.*, *11*, 263–299, doi:10.1007/BF00282579.

Forsyth, D. W. (1993), Crustal thickness and the average depth and degree of melting in fractional melting models of passive flow beneath mid-ocean ridges, *J. Geophys. Res.*, *98*, 16,073–16,079, doi:10.1029/93JB01722.

Fox, P. J., and D. G. Gallo (1984), A tectonic model for ridge-transform-ridge plate boundaries: Implications for the structure of oceanic lithosphere, *Tectonophysics*, *104*, 205–242, doi:10.1016/0040-1951(84)90124-0.

Gregg, P. M., J. Lin, M. D. Behn, and L. G. J. Montesi (2007), Spreading rate dependence of gravity anomalies along oceanic transform faults, *Nature*, *448*, 183–187, doi:10.1038/nature05962.

Grove, T. L., R. J. Kinzler, and W. B. Bryan (1992), Fractionation of mid-ocean ridge basalt, in *Mantle Flow and Melt Generation at Mid-Ocean Ridges*, *Geophys. Monogr. Ser.*, vol. 71, edited by J. Phipps Morgan et al., pp. 281–310, AGU, Washington, D. C.

Hays, M. R. (2004), Intra-transform volcanism along the Siqueiros Fracture Zone 8°20′N–8°30′N, East Pacific Rise, Ph.D. thesis, 251 pp., Univ. of Fla., Gainesville.

Hays, M. R., M. R. Perfit, D. J. Fornari, and W. Ridley (2004), Magmatism in the Siqueiros transform: Major and trace element evidence for mixing and multiple sources, *Eos Trans. AGU*, *85*(47), Fall Meet. Suppl., Abstract T41A-1165.

Hekinian, R., D. Bideau, M. Cannat, J. Francheteau, and R. Hebert (1992), Volcanic activity and crust mantle exposure in the ultrafast Garrett transform-fault near 13°28′S in the Pacific, *Earth Planet. Sci. Lett.*, *108*, 259–275, doi:10.1016/0012-821X(92)90027-S.

Hekinian, R., D. Bideau, R. Hebert, and Y. L. Niu (1995), Magmatism in the Garrett transform-fault (East Pacific Rise near 13°27′S), *J. Geophys. Res.*, *100*, 10,163–10,185, doi:10.1029/94JB02125.

Herzberg, C. (2004), Partial crystallization of mid-ocean ridge basalts in the crust and mantle, *J. Petrol.*, *45*, 2389–2405, doi:10.1093/petrology/egh040.

Hirschmann, M. M. (2000), Mantle solidus: Experimental constraints and the effects of peridotite composition, *Geochem. Geophys. Geosyst.*, *1*(10), 1042, doi:10.1029/2000GC000070.

Hooft, E. E. E., R. S. Detrick, D. R. Toomey, J. A. Collins, and J. Lin (2000), Crustal thickness and structure along three contrasting spreading segments of the Mid-Atlantic Ridge, 33.5°–35°N, *J. Geophys. Res.*, *105*, 8205–8226, doi:10.1029/1999JB900442.

Katz, R. F., M. Spiegelman, and C. H. Langmuir (2003), A new parameterization of hydrous mantle melting, *Geochem. Geophys. Geosyst.*, *4*(9), 1073, doi:10.1029/2002GC000433.

Kelemen, P. B., and E. Aharonov (1998), Periodic formation of magma fractures and generation of layered gabbros in the lower crust beneath oceanic spreading centers, in *Faulting and Magmatism at Mid-Ocean Ridges*, *Geophys. Monogr. Ser.*, vol. 106, edited by W. R. Buck et al., 348 pp., AGU, Washington, D. C.

Kinzler, R. J. (1997), Melting of mantle peridotite at pressures approaching the spinel to garnet transition: Application to mid-ocean ridge basalt petrogenesis, *J. Geophys. Res.*, *102*, 853–874, doi:10.1029/96JB00988.

Kinzler, R. J., and T. L. Grove (1992a), Primary magmas of mid-ocean ridge basalts: 2. Applications, *J. Geophys. Res.*, *97*, 6907–6926, doi:10.1029/91JB02841.

Kinzler, R. J., and T. L. Grove (1992b), Primary magmas of mid-ocean ridge basalts: 1. Experiments and methods, *J. Geophys. Res.*, *97*, 6885–6906, doi:10.1029/91JB02840.

Kinzler, R. J., and T. L. Grove (1993), Corrections and further discussion of the primary magmas of mid-ocean ridge basalts, 1 and 2, *J. Geophys. Res.*, *98*, 22,339–22,347, doi:10.1029/93JB02164.

Klein, E. M., and C. H. Langmuir (1987), Global correlations of ocean ridge basalt chemistry with axial depth and crustal thickness, *J. Geophys. Res.*, *92*, 8089–8115, doi:10.1029/JB092iB08p08089.

Kuo, B. Y., and D. W. Forsyth (1988), Gravity anomalies of the ridge transform intersection system in the South Atlantic between 31 and 34.5°S: Upwelling centers and variations in crustal thickness, *Mar. Geophys. Res.*, *10*, 205–232, doi:10.1007/BF00310065.

Langmuir, C. H., and J. F. Bender (1984), The Geochemistry of oceanic basalts in the vicinity of transform faults—Observations and implications, *Earth Planet. Sci. Lett.*, *69*, 107–127, doi:10.1016/0012-821X(84)90077-3.

Langmuir, C. H., J. F. Bender, and R. Batiza (1986), Petrological and tectonic segmentation of the East Pacific Rise, 5°30′–14°30′N, *Nature*, *322*, 422–429, doi:10.1038/322422a0.

Langmuir, C. H., E. M. Klein, and T. Plank (1992), Petrological systematics of mid-ocean ridge basalts: Constraints on melt generation beneath ocean ridges, in *Mantle Flow and Melt Generation at Mid-Ocean Ridges*, *Geophys. Monogr. Ser.*, vol. 71, edited by J. Phipps Morgan et al., pp. 183–280, AGU, Washington, D. C.

Lin, J., and J. Phipps Morgan (1992), The spreading rate dependence of three-dimensional mid-ocean ridge gravity structure, *Geophys. Res. Lett.*, *19*, 13–16, doi:10.1029/91GL03041.

Lin, J., G. M. Purdy, H. Schouten, J.-C. Sempere, and C. Zervas (1990), Evidence from gravity data for focused magmatic accretion along the Mid-Atlantic Ridge, *Nature*, *344*, 627–632, doi:10.1038/344627a0.

Maclennan, J., T. Hulme, and S. C. Singh (2005), Cooling of the lower oceanic crust, *Geology*, *33*, 357–360, doi:10.1130/G21207.1.

Magde, L. S., and D. W. Sparks (1997), Three-dimensional mantle upwelling, melt generation, and melt migration beneath segmented slow spreading ridges, *J. Geophys. Res.*, *102*, 20,571–20,583, doi:10.1029/97JB01278.

Magde, L. S., D. W. Sparks, and R. S. Detrick (1997), The relationship between buoyant mantle flow, melt migration, and gravity bull's eyes at the Mid-Atlantic Ridge between 33°N and 35°N, *Earth Planet. Sci. Lett.*, *148*, 59–67, doi:10.1016/S0012-821X(97)00039-3.

Menard, H. W. (1967), Extension of northeastern-Pacific fracture zones, *Science*, *155*, 72–74, doi:10.1126/science.155.3758.72.

Menard, H. W., and T. Atwater (1969), Origin of fracture zone topography, *Nature*, *222*, 1037–1040, doi:10.1038/2221037a0.

Menard, H. W., and R. L. Fisher (1958), Clipperton fracture zone in the northeastern equatorial Pacific, *J. Geol.*, *66*, 239–253, doi:10.1086/626502.

Michael, P. J., and W. C. Cornell (1998), Influence of spreading rate and magma supply on crystallization and assimilation beneath mid-ocean ridges: Evidence from chlorine and major element chemistry of mid-ocean ridge basalts, *J. Geophys. Res.*, *103*, 18,325–18,356, doi:10.1029/98JB00791.

Nagle, A. N., R. C. Pickle, A. E. Saal, E. H. Hauri, and D. W. Forsyth (2007), Volatiles in basalts from intra-transform spreading centers: Implications for melt migration models, *Eos Trans. AGU*, *88*(52), Fall Meet. Suppl., Abstract DI43A-05.

Niu, Y., and R. Hekinian (1997a), Spreading-rate dependence of the extent of mantle melting beneath ocean ridges, *Nature*, *385*, 326–329, doi:10.1038/385326a0.

Niu, Y. L., and R. Hekinian (1997b), Basaltic liquids and harzburgitic residues in the Garrett Transform: A case study at fast-spreading ridges, *Earth Planet. Sci. Lett.*, *146*, 243–258, doi:10.1016/S0012-821X(96)00218-X.

Parmentier, E. M., and D. W. Forsyth (1985), Three-dimensional flow beneath a slow spreading ridge axis: A dynamic contribution to the deepening of the median valley toward fracture zones, *J. Geophys. Res.*, *90*(B1), 678–684, doi:10.1029/JB090iB01p00678.

Perfit, M. R., et al. (1996), Recent volcanism in the Siqueiros transform fault: Picritic basalts and implications for MORB magma genesis, *Earth Planet. Sci. Lett.*, *141*, 91–108, doi:10.1016/0012-821X(96)00052-0.

Phipps Morgan, J., and Y. J. Chen (1993), The genesis of oceanic-crust: Magma injection, hydrothermal circulation, and crustal flow, *J. Geophys. Res.*, *98*, 6283–6297, doi:10.1029/92JB02650.

Phipps Morgan, J., and D. W. Forsyth (1988), Three-dimensional flow and temperature perturbations due to a transform offset: Effects on oceanic crustal and upper mantle structure, *J. Geophys. Res.*, *93*, 2955–2966, doi:10.1029/JB093iB04p02955.

Phipps Morgan, J., E. M. Parmentier, and J. Lin (1987), Mechanisms for the origin of mid-ocean ridge axial topography: Implications for the thermal and mechanical structure of accreting plate boundaries, *J. Geophys. Res.*, *92*, 12,823–12,836, doi:10.1029/JB092iB12p12823.

Plank, T., and C. H. Langmuir (1992), Effects of the melting regime on the composition of the oceanic crust, *J. Geophys. Res.*, *97*, 19,749–19,770, doi:10.1029/92JB01769.

Pockalny, R. A. (1997), Evidence of transpression along the Clipperton Transform: Implications for processes of plate boundary reorganization, *Earth Planet. Sci. Lett.*, *146*, 449–464, doi:10.1016/S0012-821X(96)00253-1.

Pockalny, R. A., P. J. Fox, D. J. Fornari, K. C. Macdonald, and M. R. Perfit (1997), Tectonic reconstruction of the Clipperton and Siqueiros Fracture Zones: Evidence and consequences of plate motion change for the last 3 Myr, *J. Geophys. Res.*, *102*, 3167–3181, doi:10.1029/96JB03391.

Reid, I., and H. R. Jackson (1981), Oceanic spreading rate and crustal thickness, *Mar. Geophys. Res.*, *5*, 165–172.

Reynolds, J. R., and C. H. Langmuir (1997), Petrological systematics of the Mid-Atlantic Ridge south of Kane: Implications for ocean crust formation, *J. Geophys. Res.*, *102*, 14,915–14,946, doi:10.1029/97JB00391.

Reynolds, J. R., C. H. Langmuir, J. F. Bender, K. A. Kastens, and W. B. F. Ryan (1992), Spatial and temporal variability in the geochemistry of basalts from the East Pacific Rise, *Nature*, *359*, 493–499, doi:10.1038/359493a0.

Searle, R. C. (1983), Multiple, closely spaced transform faults in fast-slipping fracture-zones, *Geology*, *11*, 607–610, doi:10.1130/0091-7613(1983)11<607:MCSTFI>2.0.CO;2.

Sparks, D. W., and E. M. Parmentier (1991), Melt extraction from the mantle beneath spreading centers, *Earth Planet. Sci. Lett.*, *105*, 368–377, doi:10.1016/0012-821X(91)90178-K.

Sparks, D. W., E. M. Parmentier, and J. Phipps Morgan (1993), Three-dimensional mantle convection beneath a segmented spreading center: Implications for along-axis variations in crustal thickness and gravity, *J. Geophys. Res.*, *98*, 21,977–21,995, doi:10.1029/93JB02397.

Tolstoy, M., A. Harding, and J. Orcutt (1993), Crustal thickness on the Mid-Atlantic Ridge: Bulls-eye gravity anomalies and focused accretion, *Science*, *262*, 726–729, doi:10.1126/science.262.5134.726.

Turcotte, D. L. (1982), Magma migration, *Annu. Rev. Earth Planet. Sci.*, *10*, 397–408, doi:10.1146/annurev.ea.10.050182.002145.

van Keken, P. E., et al. (2008), A community benchmark for subduction zone modeling, *Phys. Earth Planet. Inter.*, *171*, 187–197.

Wendt, J. I., M. Regelous, Y. L. Niu, R. Hekinian, and K. D. Collerson (1999), Geochemistry of lavas from the Garrett Transform Fault: Insights into mantle heterogeneity beneath the eastern Pacific, *Earth Planet. Sci. Lett.*, *173*, 271–284, doi:10.1016/S0012-821X(99)00236-8.

Workman, R. K., and S. R. Hart (2005), Major and trace element composition of the depleted MORB mantle (DMM), *Earth Planet. Sci. Lett.*, *231*, 53–72, doi:10.1016/j.epsl.2004.12.005.

Yang, H. J., R. J. Kinzler, and T. L. Grove (1996), Experiments and models of anhydrous, basaltic olivine-plagioclase-augite saturated melts from 0.001 to 10 kbar, *Contrib. Mineral. Petrol.*, *124*, 1–18, doi:10.1007/s004100050169.

M. D. Behn and J. Lin, Department of Geology and Geophysics, Woods Hole Oceanographic Institution, Woods Hole, MA 02543, USA.

P. M. Gregg, Department of Geosciences, Oregon State University, Corvallis, OR 97331, USA. (greggp@geo.oregonstate.edu)

T. L. Grove, Department of Earth, Atmospheric, and Planetary Sciences, Massachusetts Institute of Technology, Cambridge, MA 02139, USA.